

Nuclear many-body effects on particle emission following muon capture on ^{28}Si and ^{40}Ca

Futoshi Minato ^{1,2,*} Tomoya Naito ^{3,4} and Osamu Iwamoto¹¹*Nuclear Data Center, Japan Atomic Energy Agency, Tokai, Ibaraki 319-1195, Japan*²*RIKEN Nishina Center, Wako, Saitama 351-0198, Japan*³*RIKEN Interdisciplinary Theoretical and Mathematical Sciences Program (iTHEMS), Wako, Saitama 351-0198, Japan*⁴*Department of Physics, Graduate School of Science, The University of Tokyo, Tokyo 113-0033, Japan*

(Received 6 July 2022; revised 9 March 2023; accepted 15 May 2023; published 31 May 2023)

Background: Muon captures on nuclei have provided us with plenty of knowledge of nuclear properties. Recently, this reaction attracts attention in electronics, because charged particle emissions following muon capture on silicon become to trigger non-negligible soft errors in memory devices.

Purpose: To date, there is no theoretical framework based on the nuclear structure that describes a muon capture reaction followed by particle emissions comprehensively. The purpose of this work is to develop a new method that considers the nuclear many-body correlation for the accurate understanding of the soft errors in memory devices.

Method: We combined the second Tamm-Dancoff approximation that is used to estimate muon capture rates with the two-component exciton model, the model describing particle emission from the pre-equilibrium state. For particle evaporation from the compound state, the Hauser-Feshbach statistical models were applied. We chose ^{28}Si and ^{40}Ca to check the performance of the framework.

Result: We paid attention to the muon capture rates, the particle emission spectra, and the multiplicities that have a close interrelation with each other. We found that the nuclear many-body correlations including two-particle two-hole excitations is a key to explaining them simultaneously.

Conclusion: The present study showed that the combination of the microscopic approach of muon capture and the two-component exciton model of particle emission is an effective tool to describe particle emission following the muon captures, giving the nuclear structure information additionally. For a finer understanding of particle emission following muon capture and a validation of the present framework, further experimental studies on particle emission spectra are highly expected.

DOI: [10.1103/PhysRevC.107.054314](https://doi.org/10.1103/PhysRevC.107.054314)

I. INTRODUCTION

Negative muon capture on nuclei has recently attracted significant attention due to its various features, such as measurements of nuclear charge radii, nondestructive analyses, estimations of double β decay, and so on, as described below. The muon is first captured into outer atomic orbitals generated by the nuclear Coulomb potential and then transits to lower orbitals, emitting characteristic muonic x-rays and Auger electrons. These x-rays are utilized to determine nuclear charge radii accurately [1] and are also applied to study the proton charge radius [2]. Since the muonic x-ray spectrum with energies higher than the fluorescent x-ray is unique for elements, it is applied to nondestructive analyses inside vessels [3]. The muon eventually settles into the lowest orbital, i.e., the $1s_{1/2}$ state, and decays via $\mu^- \rightarrow e^- + \nu_\mu + \bar{\nu}_e$ or is captured by a nucleus. The latter case is analogous to electron capture of neutron-deficient nuclei, but can occur even for stable nuclei due to the large muon mass. Thus, muon capture is utilized to analyze theoretically calculated nuclear matrix

elements of double β decay [4] and neutrino-nucleus reaction on neutron-rich nuclei [4,5] that become significant in core-collapse supernovae [6].

Another importance of muon capture is to bring nuclei to highly excited states. Those nuclei deexcite by emitting various particles, some of which ionize the surrounding materials. Recently, great attention has been paid to this process in the field of electronics, because non-negligible soft errors are caused in memory devices by charged particles and recoiled nuclei that are emitted after muon capture on silicon [7]. This issue becomes more serious upon reducing the scale of memory devices (the so-called die shrink) and operating them at low voltage [8]. Because muons are constantly produced in the atmosphere by the interaction of cosmic rays and atmospheric nuclei, electric devices are always exposed to muons. Currently, soft errors in memory devices are studied with Monte Carlo transport simulations [9,10] in which, however, the muon capture process is greatly simplified by omitting to solve the nuclear many-body problem. To date, there is no theoretical framework based on the nuclear structure that comprehensively describes muon capture followed by various particle emissions, so developing a more practical model is highly demanded.

*minato.futoshi@jaea.go.jp

Particle emissions following the muon capture were extensively studied in the 70 and 80s (see review article of Ref. [11]), and it was discussed that high-energy spectra are mainly attributed to instant particle emissions from the pre-equilibrium state where excitation energy is shared only with a few nucleons in nuclei. At this stage, it was also pointed out that two-body meson-exchange current (MEC) becomes essential to explain high-energy neutron and proton emissions [12,13]. In contrast, low-energy spectra are attributed to particle evaporation from a compound state where excitation energy is shared with many nucleons in nuclei. Experimental data of particle emission spectra were explained qualitatively by phenomenological models of pre-equilibrium and compound states [13–15], independent-particle models with effective masses [16–18], and a particle-hole model considering transitions between certain nuclear levels [19]. However, they have not yet been reproduced accurately enough to be used in a practical application. Moreover, the muon capture rates were estimated with systematics and not discussed carefully from the nuclear structure point of view.

Recent theoretical studies that consider the nuclear many-body systems more appropriately pointed out that correlations resulting from the interaction between nucleons play a significant role in the muon capture [20–23]. This fact motivated us to revisit the problem of particle emission following muon capture. To understand the mechanism, we develop a new method that considers the muon capture with a microscopic nuclear model and the particle emission with an up-to-date model of pre-equilibrium and compound states. We demonstrate that many-body correlations resulting from the residual two-body interactions are essential to describe particle emission spectra and multiplicities, the number of emitted particles per a muon capture, as well as muon capture rates. In particular, the effect of two-particle two-hole (2p-2h) states, that is to say, the doorway state, is significant for the particle emission spectra. The target nucleus of this study is ^{28}Si , the main material of semiconductors. In addition, we study ^{40}Ca that have experimental data of emission spectra from low to high energies.

This paper is organized as follows: In Sec. II, we describe the model that we used to study particle emissions following muon captures. Here, we adjust neutron and proton single-particle densities used in the particle-emission model and discuss the validity of the adjustment. Section III gives the discussion of muon capture rates, particle spectra, and multiplicities, comparing with experimental data. Section IV summarizes the present work and gives future perspectives.

II. MODEL

We assume that one-neutron particle one-proton hole ($1p_{\nu}-1h_{\pi}$) states are produced in nuclei by the muon capture at first. We describe this process with the Tamm-Dancoff approximation (TDA) and second TDA (STDA), which is the extension of TDA to 2p-2h model spaces [24,25]. They are extensively applied to study nuclear states at low to high excitation energies, enabling us to examine, e.g., charge-exchange reactions. We have also tested a more sophisticated approach considering the ground-state correlation, the random-phase

approximation (RPA), and second RPA (SRPA) to calculate muon capture rates and confirmed that the results are close to those of TDA and STDA. RPA and SRPA are numerically time-consuming, so we decided in this work to adopt TDA and STDA, which are more convenient than RPA and SRPA with respect to numerical cost. We just refer to several works studying muon captures within RPA [5,20,22,26–28].

Then, we assume that the $1p_{\nu}-1h_{\pi}$ state generated by the one-body weak interaction evolves to more complicated multiparticle multihole (mp-mh) states leading to the compound state. This process, the so-called pre-equilibrium state, is still one of the challenging subjects in nuclear physics. There are mainly two approaches that have been investigated to describe the pre-equilibrium states, which are semiclassical [29] and quantum models [30] (see also Ref. [31] for the current status). The latter model has a good predictive power on several experimental data without phenomenological parameters; however, it is still difficult to comprehensively describe various kinds of multiple particle emissions in low to high energies. In contrast, the semiclassical model shows a good performance of reproducing various particle emissions with some phenomenological ingredients of partial level densities, collision matrices, and so on. We choose in this work the two-component exciton model [32,33], one of the semiclassical approaches, because various charged particle emissions are the present scope and the targets in interest are stable nuclei for which the model is well established through the nuclear data evaluations [34,35]. When nuclei reach the compound state, we describe the particle emission with the Hauser-Feshbach statistical model [36], which is also applied extensively to study nuclear reactions and particle emission after β decay [37,38].

In STDA, excited states of daughter nuclei with spin J are created by operating a phonon creation operator of the vibrational states $Q_{\lambda J}^{\dagger}$ to the target nuclear ground state $|0\rangle$ as

$$|\lambda J\rangle = Q_{\lambda J}^{\dagger}|0\rangle, \quad Q_{\lambda J}|0\rangle = 0. \quad (1)$$

We calculate the ground state $|0\rangle$ with the Skyrme-Hartree-Fock (SHF) method [39] in coordinate space assuming spherical symmetry. Note that the STDA is usually applicable for doubly magic nuclei. Although ^{28}Si has an oblate shape, the energy gap between the last occupied levels arising from $1d_{5/2}$ in the spherical shape and the first unoccupied level arising from $2s_{1/2}$ is large. In addition, the occupied levels are just resolved weakly at the oblate shape [40]. From those results, we consider that STDA can be approximately applicable to ^{28}Si . We studied with using two effective forces, which are SGII [41] and SkO' [42]. Those forces provide a reasonable strength distribution of Gamow-Teller 1^{+} and spin-dipole transitions to which muon captures are sensitive. They also reproduce the order of low-lying states of ^{28}Al and ^{40}K , the nuclei generated after the muon captures on ^{28}Si and ^{40}Ca , respectively. Continuum states are discretized by a box size $R = 14$ fm. The STDA phonon operator of the vibrational states is given by

$$Q_{\lambda J}^{\dagger} = \sum_{mi} X_{mi}^{\lambda J} \mathcal{O}_{mi}^{J\dagger} + \sum_{m \leq n, i \leq j} X_{mni}^{\lambda J} \mathcal{O}_{mni}^{J\dagger}, \quad (2)$$

where m and n denote particle states, while i and j denote hole states. The operators $\mathcal{O}_{mi}^{JM\dagger}$ and $\mathcal{O}_{mij}^{JM\dagger}$ create 1p-1h and 2p-2h states, respectively. Omitting the second term of Eq. (2) corresponds to the TDA. The coefficients X and \mathcal{X} in Eq. (2) that effectively reflect the effects of the residual two-body interaction are obtained by solving the TDA and STDA equation [24,25]

$$\begin{pmatrix} A_{11} & A_{12} \\ A_{21} & A_{22} \end{pmatrix} \begin{pmatrix} X \\ \mathcal{X} \end{pmatrix} = E_s \begin{pmatrix} X \\ \mathcal{X} \end{pmatrix}. \quad (3)$$

The matrix element A_{11} (A_{22}) includes matrix elements of residual two-body interactions that are not included in the SHF method and is responsible for interchanging one 1p-1h (2p-2h) state to another 1p-1h (2p-2h) state, while A_{12} couples one 1p-1h state with one 2p-2h state and A_{21} vice versa [25]. Setting all the matrix elements of two-body interaction in A matrices to be zero, the STDA equation is identical to the independent-particle model, which assumes nucleons freely move in the nuclear (SHF) potential. By setting A_{12} and A_{21} matrices to be zero, STDA becomes identical to TDA. The model space for 1p-1h state is set to be $\varepsilon_m - \varepsilon_i \leq 100$ MeV, where ε_m and ε_i are the single-particle energies for particle and hole states, respectively, while the model space for 2p-2h state is set to the lowest 12 levels, which are different for different nuclei and effective interactions. For ^{28}Si , the lowest 12 levels are the $2n_q + l_q \leq 2$ shell, $1f_{7/2}$, $2p$, $3s$, and $2d$ for SGII (neutron and proton) and SkO' (neutron). The lowest 12 levels for SkO' (proton) are almost the same as SkO' (neutron), but $2p_{3/2}$ is replaced by $2d_{3/2}$. For ^{40}Ca , the lowest 12 levels are the $2n_q + l_q \leq 2$ shell, $1f$, $2p$, $3s$, and $1g_{9/2}$ for SGII (neutron) and SkO' (neutron). For SGII (proton) and SkO' (proton), the lowest 12 levels are almost the same as the neutron ones, but $1g_{9/2}$ is replaced by $2p_{3/2}$. We confirmed that the result of muon capture rates converges well within this model space.

Muon capture rates are written as [20,43]

$$\begin{aligned} \omega(E) = & \sum_{\lambda,J} \frac{2G^2 v^2}{1 + v/M} \delta(E - E_x^{(\lambda,J)}) \\ & \times \left[\sum_{v\pi} X_{v\pi}^{\lambda,J} \langle j_v l_v \| \phi(\mathbf{r})(\hat{\mathcal{M}}_J - \hat{\mathcal{L}}_J) \| j_\pi l_\pi \rangle \right]^2 \\ & + \left[\sum_{v\pi} X_{v\pi}^{\lambda,J} \langle j_v l_v \| \phi(\mathbf{r})(\hat{\mathcal{T}}_J^{\text{el}} - \hat{\mathcal{T}}_J^{\text{mag}}) \| j_\pi l_\pi \rangle \right]^2, \quad (4) \end{aligned}$$

where $G = 1.166 \times 10^{-11}$ MeV $^{-2}$ is the Fermi coupling constant, M is the mass of the target nucleus, and $v = m_\mu - \Delta M + \varepsilon_\mu - E_x^{(\lambda,J)}$ is the muon neutrino energy. Here, ΔM is the mass difference between parent and descendant nuclei taken from AME2020 [44], $j_{v,\pi}$ are the total angular momentum, and $E_x^{(\lambda,J)}$ is the excitation energy with respect to the ground states of the daughter nuclei.

The muon binding energy ε_μ and the wave function $\phi(\mathbf{r})$ of the $1s_{1/2}$ orbital, the lowest state on which the muon is initially bound, are calculated by solving the Dirac equation under the Coulomb potential formed by the atomic nucleus. They are calculated by solving the Dirac equation under the Coulomb

potential formed by the atomic nucleus and the $(Z - 1)$ electrons¹

$$[T + V_{N-\mu}^{\text{Coul}}(\mathbf{r}) + V_{N-\mu}^{\text{VP}}(\mathbf{r}) + V_{e-\mu}^{\text{Coul}}(\mathbf{r})] \phi(\mathbf{r}) = \varepsilon \phi(\mathbf{r}), \quad (5)$$

where T is the Dirac kinetic operator and Z denotes the atomic number of the atom. The Coulomb potential created by the atomic nucleus reads

$$V_{N-\mu}^{\text{Coul}}(r) = -\frac{4\pi}{r} \int_0^r \bar{\rho}_{\text{ch}}(r') r'^2 dr' - 4\pi \int_r^\infty \bar{\rho}_{\text{ch}}(r') r' dr', \quad (6)$$

where $\bar{\rho}_{\text{ch}}$ is the spherical-averaged charge-density distribution of the atomic nucleus obtained by the SHF calculation, which is often approximated as the δ function in most works. The Coulomb potential formed by the $(Z - 1)$ electrons reads

$$V_{e-\mu}^{\text{Coul}}(r) = \frac{4\pi}{r} \int_0^r \rho_e(r') r'^2 dr' + 4\pi \int_r^\infty \rho_e(r') r' dr', \quad (7)$$

where ρ_e is the electron-density distribution. In this work, the electron-density distribution is calculated by the density-functional theory [45,46] with the local density approximation (LDA), where the PZ81 LDA correlation functional [47] is used. It should be noted that the electron density and the muon wave function are solved simultaneously and self-consistently; thus, the effect of the muon is also considered in the electron-density distribution as well. The vacuum polarization between the nucleus and the muon $V_{N-\mu}^{\text{VP}}$ is considered by using the Uehling effective potential [48,49].

The excitation energy $E_x^{(\lambda,J)}$ with respect to the ground states of the daughter nuclei (^{28}Al and ^{40}K) resulting from the muon capture on the parent nuclei (^{28}Si and ^{40}Ca) is approximated by $E_x^{(\lambda,J)} = E_{\text{TDA}}^{(\lambda,J)} - E_{\text{TDA}}^{(0)}$, where $E_{\text{TDA}}^{(\lambda,J)}$ and $E_{\text{TDA}}^{(0)}$ are the STDA or TDA phonon energies and the lowest energies, respectively. We consider spin-parity up to $J^\pi \leq 5^\pm$. The lowest states of TDA and STDA are, respectively, 3^+ and 4^- for ^{28}Al and ^{40}K , which are consistent with the experimental data. The one-body operators of charge $\hat{\mathcal{M}}_J$, longitudinal $\hat{\mathcal{L}}_J$, transverse electric $\hat{\mathcal{T}}_J^{\text{el}}$, and transverse magnetic $\hat{\mathcal{T}}_J^{\text{mag}}$ fields are found in Ref. [43]. The one-body operators include the axial-vector coupling, g_A , and pseudoscalar coupling, g_P . Often a smaller value of g_A in nuclei than that of the free nucleon is needed. The need of quenching arises from neglected meson-exchange currents and complex nuclear configurations [50,51]. The pseudoscalar coupling constant is derived from the Goldberger-Treiman relation [52].

A recent *ab initio* study that considers both meson-exchange currents and higher-order nuclear configurations succeeded in reproducing β -decay rates of several nuclei [53]. Although the present framework cannot fully consider the origin of the quenching, it can calculate highly excited states that are difficult to correctly describe for *ab initio* nuclear methods. We will discuss the effect of the quenching of g_A on muon capture rates, using $g_A = -1.26$ (free nucleon) and the typical quenched value of $g_A = -1$. Likewise, g_P in finite nuclei is not certain and might have a different value from that

¹Because of the charge-neutral condition, the number of bound electrons is $Z - 1$.

derived from the Goldberger-Treiman relation [54]. However, the uncertainty of g_p against muon capture rates is not as significant as that of g_A [22,26], as we show later on. For numerical purposes, the δ function in Eq. (4) is replaced by the Lorentzian function with a width of 1 MeV.

Assuming that the $1p_\nu$ - $1h_\pi$ state generated by the one-body operators of the muon capture as an initial state, we carry out the two-component exciton model calculation. The master equation of the two-component exciton model is [33]

$$\begin{aligned} \frac{dP(p_\pi, p_\nu, t)}{dt} &= P(p_\pi - 1, p_\nu, t)\lambda_{\pi+}(p_\pi - 1, p_\nu) \\ &+ P(p_\pi, p_\nu - 1, t)\lambda_{\nu+}(p_\pi, p_\nu - 1) \\ &+ P(p_\pi - 1, p_\nu + 1, t)\lambda_{\nu\pi}(p_\pi - 1, p_\nu + 1) \\ &+ P(p_\pi + 1, p_\nu - 1, t)\lambda_{\pi\nu}(p_\pi + 1, p_\nu - 1) \\ &- P(p_\pi, p_\nu, t)[\lambda(p_\pi, p_\nu) + W(p_\pi, p_\nu)], \end{aligned} \quad (8)$$

where $\lambda(p_\pi, p_\nu) = \sum_x \lambda_x(p_\pi, p_\nu)$ is the total transition rate, λ_{q+} is the creation rate of a particle-hole pair, $\lambda_{\pi\nu}$ is the exchange rate of proton and neutron particle-hole pairs, and $P(p_\pi, p_\nu, t)$ is the occupation probability of the exciton state having proton particle number p_π and neutron particle number p_ν at time t . The creation and exchange rates are given in Eqs. (169), (170), (174), and (175) of Ref. [33]. The total particle emission rate is $W(p_\pi, p_\nu) = \sum_b \int d\epsilon W_b(p_\pi, p_\nu, \epsilon)$, where W_b is the particle- b emission rate from the (p_π, p_ν) exciton state, which is calculated with the inverse reaction cross section and the partial level density for residual nuclei. In other papers studying two-exciton models, e.g., Ref. [32], the notation of hole states, $h_{\pi,\nu}$, is explicitly shown in the master equation of the two-component exciton model, but we omitted it in Eq. (8) for simplicity. By solving Eq. (8) with an initial condition of $1p_\nu$ - $1h_\pi$, the probability for emitting particle b can be calculated by [33]

$$\sigma_b(\epsilon) = \int dE R(E) \sum_{p_\pi, p_\nu} Q(p_\pi, p_\nu) W_b(p_\pi, p_\nu, \epsilon), \quad (9)$$

where Q is the cumulative occupation probability defined as [33]

$$Q(p_\pi, p_\nu) = \int_{t_0}^{t_1} P(p_\pi, p_\nu, t) dt, \quad (10)$$

and R the normalized capture rate [33]

$$R(E) = \omega(E) \frac{1}{\int \omega(E') dE'}. \quad (11)$$

As the number of excitons, which is equal to the number of particles and holes, is greater than N_{comp} , the calculation of the pre-equilibrium state terminates and that of the compound state initiates. We set $N_{\text{comp}} = 12$, which from our experience gives the best agreement with double-differential cross sections of nucleon-nucleus reactions systematically. We use a standard parameter set for pre-equilibrium and compound states that is globally used in evaluating nuclear data (see Ref. [33] for more detail). Only for the proton and neutron single-particle state densities g do we adjust to $g_\pi = Z/19$

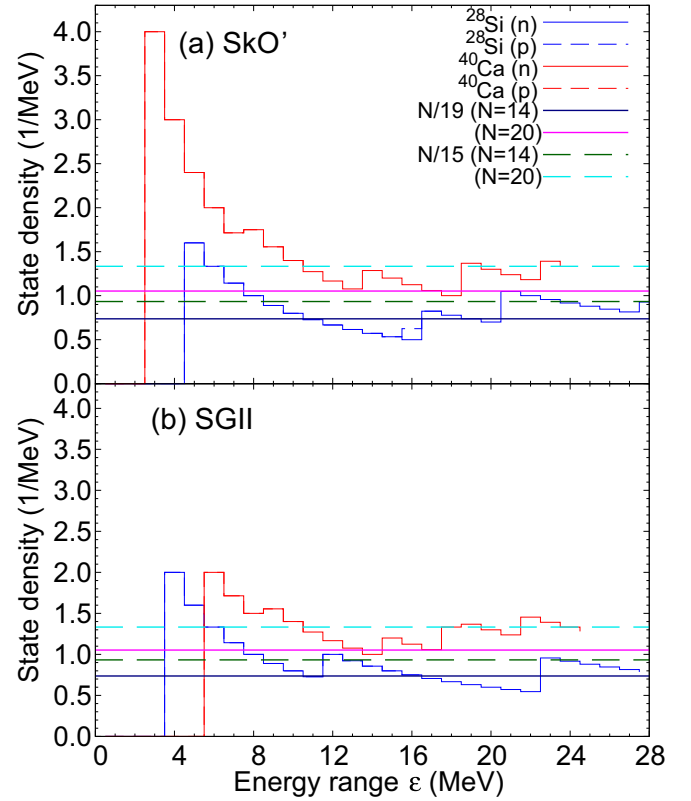


FIG. 1. Single-particle state densities of SGII (top) and SkO' (bottom) as a function of energy range ϵ . Note that those of neutron and proton are almost overlapped.

and $g_\nu = N/19$ from the standard value of the Fermi gas, $g_\pi = Z/15$ and $g_\nu = N/15$ [55]. This adjustment is reasonable considering the semimagic structure of ^{28}Si and the magic structure of ^{40}Ca .

To validate the single-particle state densities used here, we estimated them with SHF, which approximates to

$$w(\epsilon) = \frac{1}{\epsilon} \int_{\epsilon_f - \epsilon/2}^{\epsilon_f + \epsilon/2} \sum_i n_i \delta(\epsilon_i - \epsilon') d\epsilon', \quad (12)$$

where ϵ_f is the Fermi energy, ϵ_i is the single-particle energy of bound state calculated by SHF, and $n_i = 2j_i + 1$ is the degeneracy. The Fermi energy is computed by averaging the single-particle energies of the last occupied and first unoccupied levels. The results of the single-particle state density with an energy bin $\Delta\epsilon = 0.5$ MeV is shown in Fig. 1, where those for $N/15$ and $N/19$ are also drawn. Note that the results of neutrons and protons are almost overlapped because their shell structures are nearly the same due to $N = Z$. Since the level structure is discrete, the state density at $\epsilon \approx 0$ is zero. The state density becomes finite when at least one single-particle state is involved within $\epsilon_f \pm \epsilon/2$. Actually, it is vague what to the extent that we should include energy range of ϵ to determine an appropriate single-particle state density. However, we may exclude small ϵ where only a few levels are involved and large ϵ where the level is too far from ϵ_f . It may be reasonable to select $\epsilon > 8$ MeV where the state density settles down to some extent and $\epsilon < 18$ MeV since ϵ_f for

TABLE I. Calculated muon capture rates for ^{28}Si and ^{40}Ca (in the unit of 10^6 s^{-1}). The lower and upper values of model calculations are obtained by using $g_A = -1$ and -1.26 in the case of $g_P = 7$ [52], respectively. The experimental data for natural silicon and calcium are also listed [56]. The numbers in parentheses are the uncertainties of the corresponding last digits.

Nucleus	Force	FREE	TDA	STDA	Expt.
^{28}Si	SGII	1.02–1.46	0.87–1.26	0.81–1.18	0.8712(18)
	SkO'	1.04–1.49	0.87–1.26	0.72–1.04	
^{40}Ca	SGII	3.12–4.35	2.54–3.58	2.35–3.32	2.557(14)
	SkO'	2.58–3.63	2.07–2.95	1.90–2.58	

proton is about 9 MeV. We can see that the line of $N/19$ is closer to the calculated state densities in the wide range of $10 \leq \varepsilon \leq 18$ MeV than $N/15$.

III. RESULT AND DISCUSSION

Table I lists the calculated muon capture rates of ^{28}Si and ^{40}Ca . In addition to TDA and STDA, we also show the result of “FREE” that is obtained by assuming that nucleons move independently in the nuclear potential. The experimental data for natural silicon and calcium are also listed. Note that the natural abundances of ^{28}Si and ^{40}Ca are about 92% and 97%, respectively, and their muon capture rates are expected to be close to those for the natural elements. The range of calculated muon capture rates in Table I is estimated with the axial-vector coupling of $g_A = -1$ and -1.26 . In this range, the muon capture rates decrease with increasing g_A . Hence, the lower and upper values of the calculated muon capture rates correspond to the results of $g_A = -1$ and -1.26 , respectively. Here, we set $g_P = 7$ from the Goldberger-Treiman relation [52]. We find that the muon capture rates of FREE overestimate experimental data of ^{28}Si and ^{40}Ca both for SGII and SkO', while TDA and STDA reproduce them reasonably well within the uncertainties of g_A . In the case of STDA, the capture rates are systematically smaller than TDA. This is because STDA considers 2p-2h excitations, major higher-order configurations next to 1p-1h ones, and probabilities generating high nuclear excitation energies increase, leading to the reduction of phase spaces of muon neutrinos. In the case of TDA, we need to use $g_A \simeq -1$ for ^{28}Si and ^{40}Ca of SGII to match the calculated results with the experimental data, and $g_A = -1.15$ for ^{40}Ca of SkO'. However, owing to the effect of 2p-2h excitations for STDA, the axial-vector coupling constants needed to accommodate the calculated results with the experimental data shift to lower values, which are, in the case of SGII (SkO'), $g_A = -1.04$ (-1.12) for ^{28}Si and -1.06 (-1.25) for ^{40}Ca , respectively. This result indicates that a weak quenching of the axial-vector coupling constant is favorable if 2p-2h excitations are considered. We also see that the muon capture rates of SkO' is smaller than SGII. This is because the resonances for SkO' distribute at higher energies than SGII, leading to the reduction of phase spaces of muon neutrinos (see also Figs. 2 and 3). The dependence of the effective interactions is strong for ^{40}Ca , for which the muon capture rate of SkO' is about 20% lower than that of SGII.

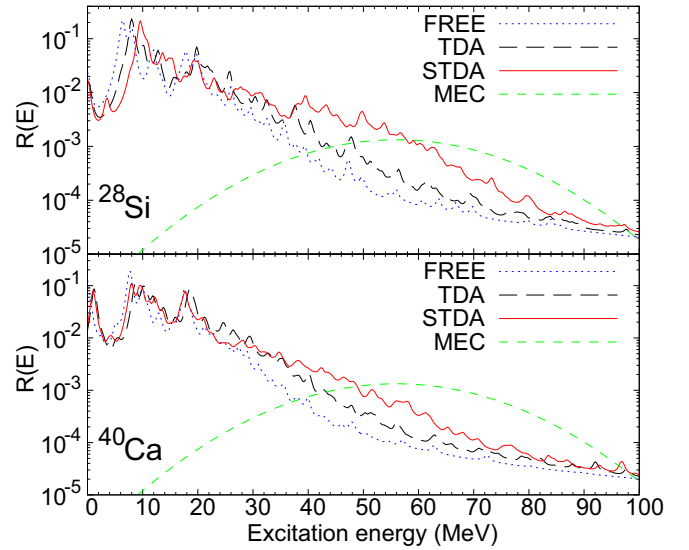


FIG. 2. Normalized capture rates $R(E)$ for ^{28}Si (top) and ^{40}Ca (bottom) obtained by FREE, TDA, and STDA. The results of SkO' force with $g_A = -1.0$ and $g_P = 7$ are shown. The horizontal axis represents the excitation energy of ^{28}Al and ^{40}K . Contributions of MEC approximated by a Gaussian form are also shown by the dashed line (see text).

Table II shows the muon capture rates for ^{28}Si and ^{40}Ca calculated within TDA and STDA varying $g_P = 0, 7, \text{ and } 10$ as done in Ref. [22]. Here, we set $g_A = -1.26$. The range of 0–10 of g_P is arbitrarily chosen just for investigating the dependence of muon capture rates. We can see that the muon capture rates decrease with increasing g_P . This dependence is consistent with the result of ^{100}Mo studied by Jokiniemi *et al.* [22]. If $g_P < 7$, the calculated muon capture rates are systematically greater than the experimental data listed in Table I. In this case, a quenched axial-vector coupling constant $g_A > -1.26$ that leads to smaller muon capture rates is required to reproduce the experimental data. On the other

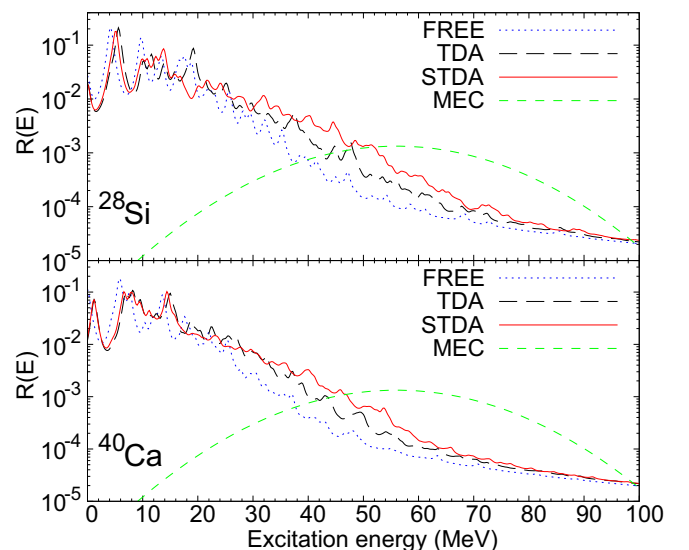


FIG. 3. Same as Fig. 2 but for the result of SGII.

TABLE II. Muon capture rates for ^{28}Si and ^{40}Ca (in units of 10^6 s^{-1}), varying the pseudoscalar coupling constant $g_P = 0, 7$, and 10. Here, we set $g_A = -1.26$.

Nucleus	Force	TDA			STDA		
		$g_P = 0$	7	10	$g_P = 0$	7	10
^{28}Si	SGII	1.44	1.26	1.20	1.35	1.18	1.12
	SkO'	1.45	1.26	1.20	1.19	1.04	0.99
^{40}Ca	SGII	4.14	3.58	3.41	3.84	3.32	3.16
	SkO'	3.42	2.95	2.81	2.99	2.58	2.46

hand, if $g_P > 7$, the calculated muon capture rates approach the experimental data, and therefore a strong quenching of g_A as the case of $g_P < 7$ is not required. Due to the uncertainty of g_P and the effective interaction dependence, it is actually difficult to make a rigorous conclusion about the relationship between the quenching of g_A and the 2p-2h excitations from the muon capture rates. However, we see that the 2p-2h excitations play a crucial role to enhance muon capture rates at high nuclear excitation energies, leading to high-energy particle emissions.

In Table I, we have seen the improvements in the muon capture rates from FREE to TDA and STDA. This result is related to the many-body correlations resulting from the residual two-body interaction. To explain it, we show in Fig. 2 the normalized capture rates $R(E)$ of ^{28}Si and ^{40}Ca calculated by SkO'. The normalized capture rates become large in lower excitation energies because outgoing muon neutrinos can have a large phase space. The functions of $R(E)$ for FREE, TDA, and STDA show a similar curve to each other in excitation energies less than about 20 MeV, although those of TDA and STDA distribute in higher energies than FREE by a few MeV. With increasing excitation energies, the capture rates decrease. Above excitation energies more than about 25 MeV, $R(E)$ become less than 0.01, and significant differences begin to emerge for FREE, TDA, and STDA. This is because the residual two-body interaction that is not taken into account for FREE works repulsively for strength distributions of most J^π channels. Such a feature substantially decreases the momentum of outgoing muon neutrino, reducing the muon capture rates through the factor v^2 in Eq. (4).

STDA gives additional enhancements in normalized muon capture rates above $E = 30$ MeV as compared with TDA as seen in Fig. 2. This is because the 1p-1h states couple with the 2p-2h ones, and some of them at high energies receive substantial strengths from those at low energies. The enhancement of transition probabilities at high energies induces the further reduction of muon capture rates as found in Table I, and a weak quenching of g_A shows a favorable agreement with the experimental data, accordingly. In general, the effect of the residual interaction becomes small with increasing energy, and the capture rates of FREE, TDA, and STDA get closer to each other.

The result of muon capture rates calculated by SGII is shown in Fig. 3. Similar to SkO', we can observe that the residual two-body interaction and the coupling with 2p-2h states induce a significant increment in muon capture rates

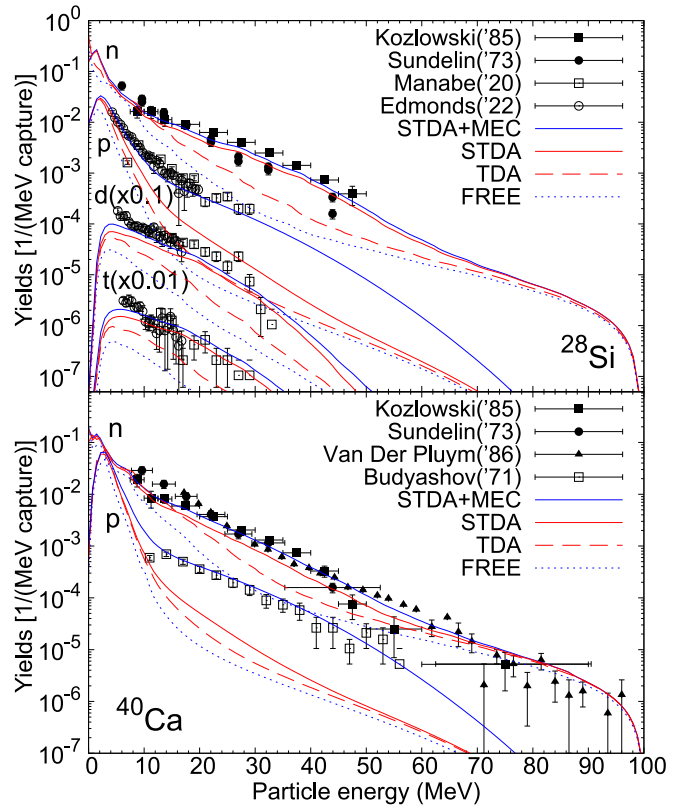


FIG. 4. Particle yields after the muon capture on ^{28}Si (top) and ^{40}Ca (bottom). The result of SkO' for $g_A = -1$ and $g_P = 7$ is shown. Experimental data for neutrons (filled symbols) and protons (open symbols) are taken from Refs. [18,57,58] and [59–61], respectively. Note that the units are not given in the original paper of Budyashov [59], so that we normalized the second point from the low energy to STDA+MEC.

above $E \geq 20$ MeV. Although the enhancement in $30 \leq E \leq 60$ MeV due to the coupling with 2p-2h states is slightly weaker than SkO', it significantly affects the particle emission spectra and multiplicities, as we discuss next.

Figure 4 shows the particle emission spectra of muon capture on ^{28}Si and ^{40}Ca . The results of SkO' with the axial-vector coupling $g_A = -1$ and $g_P = 7$ are illustrated together with the experimental data. We have checked the sensitivity of particle emission spectra to g_A and g_P . They varied only by a few percent in the range discussed in Tables I and II. In Fig. 4, the low-energy peaks formed around $E = 2-4$ MeV result from the particle emission from the compound state, while the high-energy tails of spectra are due to particle emission from the pre-equilibrium state. The result of FREE largely underestimates the experimental data. This shortcoming is improved by TDA because of the enhancement of the capture rates at high energies, as seen in Fig. 2. STDA further raises the calculated spectra and the results get closer to the experimental data. We would like to stress here that the effect of the 2p-2h excitations was small for the normalized muon capture rates, as seen in Figs. 2 and 3; however, its influence on particle emission spectra (Fig. 4) is non-negligible. We have also calculated the particle emission spectra with the single-particle state densities of $g_\pi = Z/15$ and $g_\nu = N/15$.

However, the result largely underestimated the experimental data of particle emission spectra at high energies because the large single-particle state densities prompt rapid transition to the compound state, hindering high-energy spectra attributed from the pre-equilibrium state.

STDA still largely underestimates the proton spectra in Fig. 4. The one-body operators of muon capture in Eq. (4) create only the $1p_v-1h_\pi$ state as an initial state after muon capture reactions. To enhance the proton emission spectra from this initial state, a neutron must give its energy instantly to a proton; however, this energy transfer does not occur regularly during the pre-equilibrium process. In this respect, Lifshitz and Singer have discussed the effect of MEC on proton emission spectra [13]: MEC is a two-body current and has a form of isospin operator $[\tau_1 \otimes \tau_2]^{1,-1}$, yielding $1p_\pi-2h_\pi-1p_v-0h_v$ states (hereafter called M1) and $0p_\pi-1h_\pi-2p_v-1h_v$ states (M2). The former configuration has one-proton particle at the initial state and is able to accelerate high-energy proton emissions. Lifshitz and Singer studied that the muon capture rates attributing from MEC are about 5% of the total ones for nuclei with $A < 100$ (see Table 1 of Ref. [13]) and its nuclear excitation function forms a one-peak structure (see Fig. 2 of Ref. [13]) with the mean excitation energy of 54.8–58.1 MeV. Following their discussion, we initiate the calculation of pre-equilibrium process with the initial states of M1 and M2 and see the change of particle yields after the muon captures within our framework. New particle yields are then given by

$$\sigma_{b,STDA+MEC}(\epsilon) = \sigma_{b,STDA}(\epsilon) + \frac{\mathcal{N}_M}{2} \sum_{X=1,2} \sigma_{b,MX}(\epsilon), \quad (13)$$

where

$$\sigma_{b,MX}(\epsilon) = \int dEG(E) \sum_{p_\pi, p_v} Q_{MX}(p_\pi, p_v) W_b(p_\pi, p_v, \epsilon). \quad (14)$$

The first term of Eq. (13) corresponds to particle yields calculated with the initial configuration of $1p_v-1h_\pi$ state, while the second term of Eq. (13) corresponds to particle yields calculated with the initial states of M1 and M2. The normalized muon capture rates defined as $G(E)$ in Eq. (14) is approximated by the Gaussian function. The ratio of the muon capture rates for MEC to the total one, denoted \mathcal{N}_M , is set to be 0.05. The factor of 1/2 in the second term of Eq. (13) comes from the assumption that M1 and M2 states are created with an equal probability by MEC. To hold the total muon capture rates estimated by STDA, $R(E)$ is modified to $0.95R(E)$ being $\sigma_{b,STDA} = 0.95\sigma_b$. The mean excitation energy of the Gaussian function is set to be 56 MeV and the width is arbitrarily set to 15 MeV, which is determined from an estimation of Fig. 2 of Ref. [13]. We checked the width dependence of particle yields; however, no significant differences appear below 50 MeV where one can compare with experimental data. The partial muon capture rates of MEC calculated in this way are illustrated in Fig. 2. The result of considering MEC (STDA + MEC) is shown in Fig. 4. Particle emission spectra at high energies are enhanced further, in particular, a remarkable improvement is obtained for the proton spectra in spite of the rough approximation for

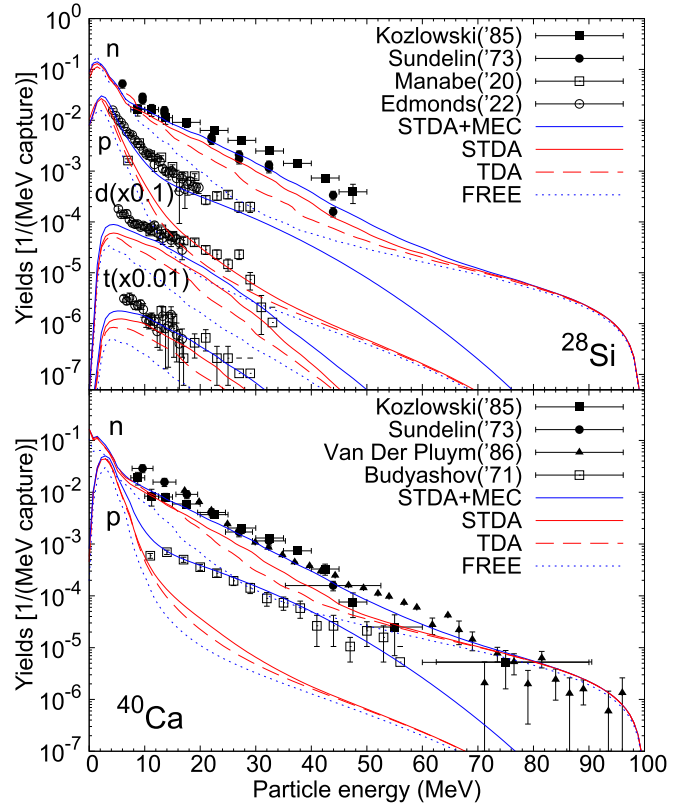


FIG. 5. Same as Fig. 4 but for the result of SGII.

MEC. This result is consistent with previous work [13], indicating that not only one-body excitations given in Eq. (4) but also MEC is essential to simulate particle emission spectra.

Figure 5 shows the particle emission spectra calculated by SGII. The results are qualitatively the same as SkO' (Fig. 3), the calculated spectra at high energies are slightly smaller than SkO'. However, we can see that the effect of the coupling with $2p-2h$ states is non-negligible. Together with MEC, the calculated spectra show a good agreement with the experimental data.

Table III lists the calculated and experimental data of multiplicities of emitted particles for ^{28}Si and ^{40}Ca , which are obtained by integrating particle yields with energy. Here, we used $g_A = -1$ and $g_P = 7$ in the calculation; however, we confirmed that the difference from $g_A = -1.26$ is less than 3%. The results of FREE underestimate the experimental data, while we obtain improvements with increasing the many-body correlations of $1p-1h$ mixture (TDA), and the coupling with $2p-2h$ states (STDA). The effect of MEC is comparable to TDA and STDA, making the calculated results even closer to the experimental data. On the contrary, the calculated α -particle multiplicity of ^{28}Si and neutron multiplicity of ^{40}Ca deviate from the experimental data. The measured energy range of α -particle multiplicity for ^{28}Si is limited only to 15–20 MeV and the available experimental data of neutron multiplicity for ^{40}Ca is only one, which was measured more than 50 years ago [62]. The multiplicity strongly depends on the distribution of capture rates that modulates particle

TABLE III. Calculated multiplicities per 10^3 muon captures for ^{28}Si and ^{40}Ca compared with the experimental data for the natural silicon and calcium. The results of SGII and SkO' forces with $g_A = -1$ and $g_P = 7$ are shown. Experimental data for neutrons are taken from Ref. [62], while those for charged particles are from Ref. [60]. Energy ranges experimentally measured in Ref. [62] are shown in the third column. We regarded neutron spectra of Ref. [60] are measured in an entire energy region. The numbers in parentheses are the uncertainties of the corresponding last digits.

Nucleus	Particle	Energy range (MeV)	FREE		TDA		STDA		STDA + MEC		Expt.
			SGII	SkO'	SGII	SkO'	SGII	SkO'	SGII	SkO'	
^{28}Si	n	Entire	639	573	631	812	676	938	729	983	864(72)
	p	4–20	14.9	13.5	23.9	23.7	31.8	41.4	54.4	63.5	52.46(192)
	d	5–17	1.99	2.01	3.98	4.13	5.89	7.13	7.96	9.15	9.80(46)
	t	6–17	0.303	0.309	0.714	0.720	1.18	1.54	1.63	1.97	1.70(13)
	α	15–20	0.288	0.285	0.598	0.607	0.944	1.14	1.28	1.47	0.57(10)
^{40}Ca	n	Entire	352	473	583	659	559	631	613	681	764(32)

emissions from the pre-equilibrium state, which emits only a few particles, and the compound state, which emits multiple particles. For further understanding of particle emissions and validations of the nuclear model, more experimental studies that cover the spectra from low to high energies are required.

Here, we show the calculated multiplicities of charged particles for entire energy range in Table IV, where $g_A = -1$ and $g_P = 7$ is used in the calculation. We confirmed that the difference from $g_A = -1.26$ is less than 3%. Compared with Table III, the multiplicities of charged particles in the entire energy region are considerably larger, implying that the measured energy ranges are still narrow to discuss the influences on memory devices. In particular, the α -particle multiplicity in entire energy region is 40–50 times larger than that of $15 \leq E \leq 20$ MeV of Table III. This result means that further experimental investigations are still needed.

IV. SUMMARY

We demonstrated that the many-body correlation resulting from the residual two-body interaction operating between nucleons plays an important role in the muon capture rates of ^{28}Si and ^{40}Ca . In particular, the coupling with $2p$ - $2h$ states is essential to describe the particle emission spectra and the mul-

tiplicities. In other words, this indicates that particle emissions following muon captures have information on the nuclear structure at high energies. The present study shows that the combination of the microscopic approach of muon capture and the two-component exciton model of particle emission is an effective tool to describe particle emission following muon capture, giving additional nuclear structure information. Only the effect of MEC was considered within a simple manner, so that it is demanded in future to take it into account within the framework of STDA that is able to calculate transition amplitudes of two-body external field of MEC given in Refs. [13,63,64] in nuclear many-body systems. The present outcomes are expected to contribute to the development of Monte Carlo transport simulations of muon captures [9,10] and further understanding of the nuclear structure.

The α -particle multiplicity of ^{28}Si and neutron multiplicity of ^{40}Ca are the remaining questions of this work. Currently, three facilities providing negative muon beams (TRIUMF, RAL, J-PARC, and PSI) are running in the world, and new experiments are planned there. In addition, a new negative muon facility is going to launch in RCNP at Osaka University. Those activities will increase information on the interaction between muon and nuclei, and help us not only to verify the present framework but also to develop theoretical models.

TABLE IV. Calculated multiplicities per 10^3 muon captures for ^{28}Si and ^{40}Ca in the case of the entire energy range. The results of SGII and SkO' forces with the axial-vector coupling $g_A = -1$ and pseudoscalar coupling $g_P = 7$ are shown.

Nucl.	Emitted particle	FREE		TDA		STDA		STDA+MEC	
		SGII	SkO'	SGII	SkO'	SGII	SkO'	SGII	SkO'
^{28}Si	p	60.7	61.5	94.2	98.9	101	119	128	144
	d	2.51	2.49	4.68	4.91	6.71	8.66	9.32	11.2
	t	0.442	0.448	0.940	0.979	1.52	2.07	2.16	2.68
	^3He	0.0512	0.0540	0.127	0.130	0.230	0.368	0.383	0.514
	α	12.5	11.5	18.2	18.0	20.3	24.4	24.7	28.6
^{40}Ca	p	101	136	169	221	166	203	202	238
	d	2.28	2.62	5.01	5.58	5.42	5.87	7.74	8.17
	t	0.286	0.331	0.733	0.808	0.934	1.07	1.46	1.58
	^3He	0.0948	0.110	0.250	0.276	0.339	0.397	0.548	0.630
	α	25.7	25.5	39.3	42.4	38.5	39.6	42.0	43.0

ACKNOWLEDGMENTS

The authors thanks Professor S. Kawase, Dr. A. Abe, and Professor G. Colò for fruitful discussion. F.M. thanks Dr. T. Fukui for supporting this work. T.N. thanks Dr. S. A. Sato for the discussion on the code for electron wave functions in the density functional theory. T.N. acknowledges the JSPS Grant-in-Aid for Research Activity Start-up under Grant No. 22K20372, the RIKEN Special Postdoctoral Researchers

Program, and the Science and Technology Hub Collaborative Research Program from RIKEN Cluster for Science, Technology and Innovation Hub (RCSTI) the JSPS Grant-in-Aid for Transformative Research Areas (A) under Grant No. 23H04526, the JSPS Grant-in-Aid for Scientific Research (B) under Grant No. 23H01845. The numerical calculations were partly performed on cluster computers at the RIKEN iTHEMS program.

-
- [1] G. Fricke, C. Bernhardt, K. Heilig, L. A. Schaller, L. Schellenberg, E. B. Shera, and C. W. De Jager, Nuclear ground state charge radii from electromagnetic interactions, *At. Data Nucl. Data Tables* **60**, 177 (1995).
- [2] A. Antognini *et al.*, Proton structure from the measurement of 2S-2P transition frequencies of muonic hydrogen, *Science* **339**, 417 (2013).
- [3] K. Shimada-Takaura, K. Ninomiya, A. Sato, N. Ueda, M. Tambo, S. Takeshita, I. Umegaki, Y. Miyake, and K. Takahashi, A novel challenge of nondestructive analysis on OGATA Koan's sealed medicine by muonic X-ray analysis, *Nat. Med. (Tokyo, Jpn.)* **75**, 532 (2021).
- [4] I. H. Hashim and H. Ejiri, Ordinary muon capture for double beta decay and anti-neutrino nuclear responses, *Front. Astron. Space Sci.* **8**, 666383 (2021).
- [5] E. Kolbe, K. Langanke, and K. Riisager, Muon capture on neutron-rich nuclei, *Eur. Phys. J. A* **11**, 39 (2001).
- [6] T. Suzuki, Nuclear weak rates and nuclear weak processes in stars, *Prog. Part. Nucl. Phys.* **126**, 103974 (2022).
- [7] S. Serre, S. Semikh, S. Uznanski, J. L. Autran, D. Munteanu, G. Gasiot, and P. Roche, Geant4 analysis of n-Si nuclear reactions from different sources of neutrons and its implication on soft-error rate, *IEEE Trans. Nucl. Sci.* **59**, 714 (2012).
- [8] W. Liao, M. Hashimoto, S. Manabe, S.-I. Abe, and Y. Watanabe, Similarity analysis on neutron- and negative muon-induced MCUs in 65-nm bulk SRAM, *IEEE Trans. Nucl. Sci.* **66**, 1390 (2019).
- [9] S.-i. Abe and T. Sato, Implementation of muon interaction models in PHITS, *J. Nucl. Sci. Technol. (Abingdon, U. K.)* **54**, 101 (2017).
- [10] M. V. Kossov, Chiral invariant phase space event generator, *Eur. Phys. J. A* **33**, 7 (2007).
- [11] D. F. Measday, The nuclear physics of muon capture, *Phys. Rep.* **354**, 243 (2001).
- [12] F. Dautry, M. Rho, and D. O. Riska, Weak interactions in deuterons: Exchange currents and nucleon-nucleon interaction, *Nucl. Phys. A* **264**, 507 (1976).
- [13] M. Lifshitz and P. Singer, Meson-exchange currents and energetic particle emission from μ^- capture, *Nucl. Phys. A* **476**, 684 (1988).
- [14] M. Lifshitz and P. Singer, Nuclear excitation function and particle emission from complex nuclei following muon capture, *Phys. Rev. C* **22**, 2135 (1980).
- [15] N. C. Mukhopadhyay, Nuclear muon capture, *Phys. Rep.* **30**, 1 (1977).
- [16] C. Ishii, An analysis of the charged particles emitted following negative muon absorptions in photographic emulsions, *Prog. Theor. Phys.* **21**, 663 (1959).
- [17] P. Singer, Neutron emission following muon capture in heavy nuclei, *Nuovo Cimento* **23**, 669 (1962).
- [18] J. Van Der Pluym, T. Kozłowski, W. H. A. Hesselink, A. Van Der Schaaf, C. Grab, E. A. Hermes, and W. Bertl, High-energy neutrons emitted after muon capture in ^{40}Ca , *Phys. Lett. B* **177**, 21 (1986).
- [19] L. L. Hill and H. Überall, Spectra of neutrons emitted after muon capture in ^{16}O , ^{28}Si , ^{32}S and ^{40}Ca , *Nucl. Phys. A* **190**, 341 (1972).
- [20] T. Marketin, N. Paar, T. Nikšić, and D. Vretenar, Relativistic quasiparticle random-phase approximation calculation of total muon capture rates, *Phys. Rev. C* **79**, 054323 (2009).
- [21] A. Lovato, N. Rocco, and R. Schiavilla, Muon capture in nuclei: An *ab initio* approach based on Green's function Monte Carlo methods, *Phys. Rev. C* **100**, 035502 (2019).
- [22] L. Jokiniemi, J. Suhonen, H. Ejiri, and I. H. Hashim, Pinning down the strength function for ordinary muon capture on ^{100}Mo , *Phys. Lett. B* **794**, 143 (2019).
- [23] M. Ciccarelli, F. Minato, and T. Naito, Theoretical study of Nb isotope productions by muon capture reaction on ^{100}Mo , *Phys. Rev. C* **102**, 034306 (2020).
- [24] J. Da Providência, Variational approach to the many-body problem, *Nucl. Phys.* **61**, 87 (1965).
- [25] F. Minato, Estimation of a 2p2h effect on Gamow-Teller transitions within the second Tamm-Dancoff approximation, *Phys. Rev. C* **93**, 044319 (2016).
- [26] E. Kolbe, K. Langanke, and P. Vogel, Muon capture, continuum random phase approximation, and in-medium renormalization of the axial-vector coupling constant, *Phys. Rev. C* **50**, 2576 (1994).
- [27] N. T. Zinner, K. Langanke, and P. Vogel, Muon capture on nuclei: Random phase approximation evaluation versus data for $6 \leq Z \leq 94$ nuclei, *Phys. Rev. C* **74**, 024326 (2006).
- [28] L. Jokiniemi and J. Suhonen, Comparative analysis of muon-capture and $0\nu\beta\beta$ -decay matrix elements, *Phys. Rev. C* **102**, 024303 (2020).
- [29] J. J. Griffin, Statistical Model of Intermediate Structure, *Phys. Rev. Lett.* **17**, 478 (1966).
- [30] H. Feshbach, A. Kerman, and S. Koonin, The statistical theory of multi-step compound and direct reactions, *Ann. Phys. (NY)* **125**, 429 (1980).
- [31] B. V. Carlson, J. E. Escher, and M. S. Hussein, Theoretical descriptions of compound-nuclear reactions: Open problems and challenges, *J. Phys. G* **41**, 094003 (2014).
- [32] A. J. Koning and M. C. Duijvestijn, A global pre-equilibrium analysis from 7 to 200 MeV based on the optical model potential, *Nucl. Phys. A* **744**, 15 (2004).
- [33] O. Iwamoto, N. Iwamoto, S. Kunieda, F. Minato, and K. Shibata, The CCONE code system and its application to

- nuclear data evaluation for fission and other reactions, *Nucl. Data Sheets* **131**, 259 (2016).
- [34] D. M. Hetrick, D. C. Larson, N. M. Larson, L. C. Leal, and S. J. Epperson, Evaluation of $^{28,29,30}\text{Si}$ neutron induced cross sections for ENDF/B-VI, ORNL/TM-11825 (1997).
- [35] K. Shibata and S. Kunieda, Calculation of neutron nuclear data on silicon isotopes for JENDL-4, *J. Nucl. Sci. Technol. (Abingdon, UK)* **45**, 123 (2008).
- [36] W. Hauser and H. Feshbach, The inelastic scattering of neutrons, *Phys. Rev.* **87**, 366 (1952).
- [37] M. R. Mumpower, T. Kawano, T. M. Sprouse, N. Vassh, E. M. Holmbeck, R. Surman, and P. Möller, β -delayed fission in r -process nucleosynthesis, *Astrophys. J. Lett.* **869**, 14 (2018).
- [38] F. Minato, T. Marketin, and N. Paar, β -delayed neutron-emission and fission calculations within relativistic quasiparticle random-phase approximation and a statistical model, *Phys. Rev. C* **104**, 044321 (2021).
- [39] D. Vautherin and D. M. Brink, Hartree-Fock calculations with Skyrme's interaction. I. Spherical nuclei, *Phys. Rev. C* **5**, 626 (1972).
- [40] E. Ha and M.-K. Cheoun, A study of Gamow-Teller transitions for $N = Z$ nuclei, ^{24}Mg , ^{28}Si , and ^{32}S , by a deformed QRPA, *Eur. Phys. J. A* **53**, 26 (2017).
- [41] N. Van Giai and H. Sagawa, Spin-isospin and pairing properties of modified Skyrme interactions, *Phys. Lett. B* **106**, 379 (1981).
- [42] P.-G. Reinhard, D. J. Dean, W. Nazarewicz, J. Dobaczewski, J. A. Maruhn, and M. R. Strayer, Shape coexistence and the effective nucleon-nucleon interaction, *Phys. Rev. C* **60**, 014316 (1999).
- [43] J. S. O'Connell, T. W. Donnelly, and J. D. Walecka, Semileptonic weak interactions with C^{12} , *Phys. Rev. C* **6**, 719 (1972).
- [44] M. Wang, W. J. Huang, F. G. Kondev, G. Audi, and S. Naimi, The AME 2020 atomic mass evaluation (II). Tables, graphs and references, *Chin. Phys. C* **45**, 030003 (2021).
- [45] P. Hohenberg and W. Kohn, Inhomogeneous electron gas, *Phys. Rev.* **136**, B864 (1964).
- [46] W. Kohn and L. J. Sham, Self-consistent equations including exchange and correlation effects, *Phys. Rev.* **140**, A1133 (1965).
- [47] J. P. Perdew and A. Zunger, Self-interaction correction to density-functional approximations for many-electron systems, *Phys. Rev. B* **23**, 5048 (1981).
- [48] E. A. Uehling, Polarization effects in the positron theory, *Phys. Rev.* **48**, 55 (1935).
- [49] L. Wayne Fullerton and G. A. Rinker, Accurate and efficient methods for the evaluation of vacuum-polarization potentials of order $Z\alpha$ and $Z\alpha^2$, *Phys. Rev. A* **13**, 1283 (1976).
- [50] M. Ichimura, H. Sakai, and T. Wakasa, Spin-isospin responses via (p, n) and (n, p) reactions, *Prog. Part. Nucl. Phys.* **56**, 446 (2006).
- [51] I. Towner, Quenching of spin matrix elements in nuclei, *Phys. Rep.* **155**, 263 (1987).
- [52] M. L. Goldberger and S. B. Treiman, Form factors in β decay and μ capture, *Phys. Rev.* **111**, 354 (1958).
- [53] P. Gysbers, G. Hagen, J. D. Holt, G. R. Jansen, T. D. Morris, P. Navrátil, T. Papenbrock, S. Quaglioni, A. Schwenk, S. R. Stroberg, and K. A. Wendt, Discrepancy between experimental and theoretical β -decay rates resolved from first principles, *Nat. Phys.* **15**, 428 (2019).
- [54] T. Gorringer and H. W. Fearing, Induced pseudoscalar coupling of the proton weak interaction, *Rev. Mod. Phys.* **76**, 31 (2003).
- [55] A. Bohr and B. Mottelson, *Nuclear Structure Volume I: Single Particle Motion* (Benjamin, New York, 1969).
- [56] T. Suzuki, D. F. Measday, and J. P. Roalsvig, Total nuclear capture rates for negative muons, *Phys. Rev. C* **35**, 2212 (1987).
- [57] R. M. Sundelin and R. M. Edelman, Neutron asymmetries and energy spectra from muon capture in Si, S, and Ca, *Phys. Rev. C* **7**, 1037 (1973).
- [58] T. Kozłowski, W. Bertl, H. P. Povel, U. Sennhauser, H. K. Walter, A. Zglinski, R. Engfer, C. Grab, E. A. Hermes, H. P. Isaak, A. Van Der Schaaf, J. Van Der Pluym, and W. H. A. Hesselink, Energy spectra and asymmetries of neutrons emitted after muon capture, *Nucl. Phys. A* **436**, 717 (1985).
- [59] Y. G. Budyashov, V. G. Zinov, A. D. Konin, A. I. Mukhin, and A. M. Chatrchyan, Charged particles produced in capture of negative muons by ^{28}Si , ^{32}S , ^{40}Ca , and ^{64}Cu nuclei, *Sov. Phys. JETP* **33**, 11 (1971).
- [60] A. Edmonds, J. Quirk, M.-L. Wong, D. Alexander, R. H. Bernstein, A. Daniel, E. Diociaiuti, R. Donghia, E. L. Gillies, E. V. Hungerford, P. Kammel, B. E. Krikler, Y. Kuno, M. Lancaster, R. P. Litchfield, J. P. Miller, A. Palladino, J. Repond, A. Sato, I. Sarra, S. R. Soleti, V. Tishchenko, N. H. Tran, Y. Uchida, P. Winter, and C. Wu (AlCap Collaboration), Measurement of proton, deuteron, triton, and α particle emission after nuclear muon capture on Al, Si, and Ti with the AlCap experiment, *Phys. Rev. C* **105**, 035501 (2022).
- [61] S. Manabe, Ph.D. thesis, Kyushu University, 2020.
- [62] B. Macdonald, J. A. Diaz, S. N. Kaplan, and R. V. Pyle, Neutrons from negative-muon capture, *Phys. Rev.* **139**, B1253 (1965).
- [63] B. Sommer, Deuteron electrodisintegration at high energy and momentum transfer, *Nucl. Phys. A* **308**, 263 (1978).
- [64] W. Alberico, M. Ericson, and A. Molinari, The role of two particle-two hole excitations in the spin-isospin nuclear response, *Ann. Phys. (NY)* **154**, 356 (1984).